AD_____

Award Number: DAMD17-99-1-9130

TITLE: Finite Element Based Photon Migration Imaging

PRINCIPAL INVESTIGATOR: Huabei Jiang, Ph.D.

CONTRACTING ORGANIZATION: Clemson University
                            Clemson, South Carolina   29634-5702

REPORT DATE: May 2001

TYPE OF REPORT: Annual Summary

PREPARED FOR: U.S. Army Medical Research and Materiel Command
                Fort Detrick, Maryland   21702-5012

DISTRIBUTION STATEMENT: Approved for Public Release;
                          Distribution Unlimited

The views, opinions and/or findings contained in this report are
those of the author(s) and should not be construed as an official
Department of the Army position, policy or decision unless so
designated by other documentation.

20010620 199

REPORT DOCUMENTATION PAGE

1. AGENCY USE ONLY (Leave blank)	2. REPORT DATE	3. REPORT TYPE AND DATES COVERED
	May 2001	Annual Summary (1 May 00 - 30 Apr 01)

4. TITLE AND SUBTITLE
Finite Element Based Photon Migration Imaging

5. FUNDING NUMBERS
DAMD17-99-1-9130

6. AUTHOR(S)
Huabei Jiang, Ph.D.

7. PERFORMING ORGANIZATION NAME(S) AND ADDRESS(ES)
Clemson University
Clemson, South Carolina 29634-5702

E-Mail: hjiang@clemson.edu

8. PERFORMING ORGANIZATION REPORT NUMBER

9. SPONSORING / MONITORING AGENCY NAME(S) AND ADDRESS(ES)

U.S. Army Medical Research and Materiel Command
Fort Detrick, Maryland 21702-5012

10. SPONSORING / MONITORING AGENCY REPORT NUMBER

11. SUPPLEMENTARY NOTES

12a. DISTRIBUTION / AVAILABILITY STATEMENT
Approved for Public Release; Distribution Unlimited

12b. DISTRIBUTION CODE

13. ABSTRACT *(Maximum 200 Words)*

This research is aimed at developing a new optical approach, called "Photon Migration Imaging", for breast cancer detection and diagnosis. The project will develop computer software and conduct phantom experiments to achieve the proposed goals. During the second year of this project, we have continually evaluated and optimized the image enhancing schemes developed in Year 1 using tissue phantom experiments. We have improved the multi-channel frequency-domain imaging system that was constructed in Year 1. We have conducted extensive phantom experiments for fluorescence lifetime imaging. The successful experiments have confirmed the imaging capability of our reconstruction software. We have also performed successful fluorescence phantom studies that were proposed to occur in Year 3 of the project. We have for the first time obtained fluorescence lifetime images from *in vivo* animal measurements which were even not proposed to attempt in the original proposal.

14. SUBJECT TERMS
Breast Cancer, Photon Migration Imaging

15. NUMBER OF PAGES
26

16. PRICE CODE

17. SECURITY CLASSIFICATION OF REPORT	18. SECURITY CLASSIFICATION OF THIS PAGE	19. SECURITY CLASSIFICATION OF ABSTRACT	20. LIMITATION OF ABSTRACT
Unclassified	Unclassified	Unclassified	Unlimited

Table of Contents

Introduction

The ability of near-infrared (NIR) light-based techniques to noninvasively image and analyze tissue structure and function promises their great potential for detection and diagnosis of breast cancer. Optical diagnostic techniques allow us to not only enhance the existing capabilities, but to eliminate the need for physical biopsies. In addition, optical imaging is inexpensive and portable, which indicates that optical imaging could be an ideal candidate for routine breast screening. However, since the scattering properties of tissues convolute re-emitted NIR signals, the extraction of pertinent information continues to remain elusive. An understanding of light propagation and light-tissue interaction is required before the optical technologies can substantially impact diagnostic medicine.

Research efforts in the Biomedical Optics Laboratory at Clemson University are focused on the biophysics of light propagation and light-tissue interaction in order to engineer appropriate approaches for noninvasive breast imaging and spectroscopy. Specifically, we are developing indirect optical/fluorescence approaches using photon migration measurements in the continuous-wave and frequency domains. These indirect optical/fluorescence approaches or image reconstructions are computationally based on the powerful finite element methods. A CCD-based optical spectroscopic imaging system is already operational in our laboratory for continuous-wave tomographic photon migration measurements, while a frequency-domain system is still under construction. Using these optical systems coupled with our finite element based reconstruction algorithms, we will be able to extract spatial/spectroscopic maps of tissue optical properties, lifetime and/or yield of endogenous and exogenous fluorescent probes. Since metabolic tissue states can be identified by our approaches, diagnostic information is also obtained in addition to detection of tumor.

This Career Development application for support of Dr. Huabei Jiang will facilitate the establishment/continuation of these research activities. Interdisciplinary interactions with the Greenville Hospital System (Greenville, SC) will be enhanced, which insures the direction of research towards a clinically pertinent and feasible system.

Body

This report describes work accomplished during the <u>second</u> year of a proposed four-year study. This Career Award supports Dr. Jiang's research on optical and fluorescence imaging using both continuous-wave and frequency-domain measurements. The focus of the proposed work in Year 2 is the continued evaluation and optimization of some enhancing schemes in our existing 2D reconstruction codes using tissue phantom experiments; continued phantom studies of image reconstructions with dye-free or dye-laden phantom background; improvement of the imaging system that was built during the first year of this project; *in vivo* animal imaging studies using frequency-domain measurements.

Software work: We have continually evaluated and optimized the important image enhancing schemes that were implemented during the first year of the project. Extensive tissue phantom experiments have been conducted to complete these studies. The results from these studies have been published in the peer-reviewed literature (see

a manuscript entitled "Quantitative optical image reconstruction of turbid media by using direct-current measurements" provided in the *Appendix* to the Summary Report).

Hardware Development: We have attempted to improve the multi-channel frequency-domain imaging system we constructed in Year 1 in terms of the signal-to-noise ratio. What we have tried was to use a thermo-electric cooling system for the photomultiplier tubes (PMTs). This has provided 20-30% noise reduction relative to the original imaging system. We plan to continually improve the system in other areas such as the use of low loss silica optic fibers (the current system uses glass optic fibers which normally give 30-40% more losses than the silica fibers).

Phantom Experiments: Using our frequency-domain imaging system, we have conducted extensive phantom experiments for fluorescence lifetime reconstruction with dye-free background and dye-laden background which was proposed to take place during the third year of the project. Our experimental setup used was the automated multi-channel frequency-domain system mentioned above. The system employed a radio-frequency intensity-modulated near-infrared beam. The laser beam at 785 nm was sent to the phantom by 16 fiber optic bundles coupled with a high precision moving stage. The diffused radiation was received by another 16 channel fiber optic bundles and delivered to a thermo-electric cooled PMT. A second PMT was used to record the reference signal. These PMTs were supplied at a radio-frequency modulated current with 0.1-1KHz shift. The intermediary frequency signal obtained from the PMTs was processed using a National Instruments board. To increase the dynamic range of intensities that the PMT can detect, an automated filter wheel with pre-calibrated neutral density filters was added to the system. For every source position, 16 measurements for each detector were made, taking alternatively 100 ms samples for sample and reference signals. Fluorescence signals were obtained through an 830nm interference filter placed in front of the detection PMT. ac intensity and phase shift between reference and sample signals were obtained using FFT Labview routines. The total data collection time for 256 measurements was 8 minutes.

Solid phantom was used to mimic the human tissue. It was made of agar, Intralipid, black ink and fluorescent dyes. The absorption and the reduced scattering coefficients are linear with the ink and Intralipid concentrations, respectively. Micromolar ICG and DTTCI dyes were added in the tissue phantom to provide the fluorescence contrast. Agar is used to make the phantom solid. The solid phantom consisted of a cylindrical background and a cylindrical heterogeneity. The absorption peaks of ICG and DTTCI are 764 nm and 780 nm, respectively. And the fluorescent emission peaks of them are 803 nm and 830 nm respectively. Their lifetimes in water were measured to be 0.56 ns and 1.18 ns, respectively. A laser diode of wavelength 785 nm was used to excite both dyes, and the emission light of wavelength at 830 nm were detected for both of them through an interference filter of center wavelength 830 nm with 10nm bandwidth. The image results have been presented in the second and third manuscripts provided in the *Appendix* to this Summary Report.

Initial In vivo Experiments: We have tested our overall reconstruction approach using in vivo animals which we originally planned to pursue after the funded four-year study. While we may be able to conduct another *in vivo* experiment within the course of this project, this initial animal study has surely provided us an excellent opportunity to test

the feasibility of the proposed research approach for breast imaging. In the *in vivo* experiments, Wistar furth female rats with MT/W9a-B (mammary carcinosarcoma) cell line developed in their right udder were used as the animal models. Animals were studied when the tumor sizes were around 10~30 mm diameters. Animals were initially anesthetized with 2% isoflurane. The femoral vein was cannulated for the administration of intravenous drugs, including the dye ICG. Anesthesia was maintained during the experiment. The animals were placed in a holder with their tumor positions placed into the measuring ring. 1.5 mg/Kg bodyweight of ICG dye was injected into the animal. Imaging studies were carried out after 2 minutes of the dye injection. Successful *in vivo* image results have been reported in the third manuscript provided in the *Appendix*.

Key Research Accomplishments

1. We have continually evaluated and optimized the image enhancing schemes developed in Year 1 using tissue phantom experiments.
2. We have improved the multi-channel frequency-domain imaging system that was constructed in Year 1.
3. We have conducted extensive phantom experiments for fluorescence lifetime imaging. The successful experiments have confirmed the imaging capability of our reconstruction software. We have also performed successful fluorescence phantom studies that were proposed to occur in Year 3 of the project.
4. We have for the first time obtained fluorescence lifetime images from *in vivo* animal measurements which were even not proposed to attempt in the original proposal.

Reportable Outcomes (see the Appendix to this Summary Report)

Conclusions

We have made a significant progress that has exceeded the statement of work proposed for Year 2 of this project. Given the successful first year, we will be able to fulfil or exceed the work statement for Year 3, and we will carry these successful works over into the final year of this project.

Appendix

1. N. Iftimia, H. Jiang, "Quantitative optical image reconstruction of turbid media by using direct-current measurements", *Appl. Opt.* **39**, 5256-5261(2000).

2. Huabei Jiang, Sathappan Ramesh, Matthew Bartlett, "Combined optical and fluorescence imaging for breast cancer detection and diagnosis", *Critical Rev. in Biomed. Engr.* **28**, 371-375(2000).

3. Ye Yang, Nicusor Iftimia, Yong Xu, Huabei Jiang, "Frequency-domain fluorescent diffusion tomography of turbid media and *in vivo* tissues", *Proc. of SPIE* **4250** (in press), 2001.

Quantitative optical image reconstruction of turbid media by use of direct-current measurements

Nicusor Iftimia and Huabei Jiang

We present a detailed experimental study concerning quantitative optical property reconstruction of heterogeneous turbid media by use of absolute dc data only. We performed experiments by using tissuelike phantoms in both single-target and multitarget configurations in which variations in target size and optical contrast with the background were explored. Our results show that both scattering and absorption images can be reconstructed quantitatively by use of dc data only, whereas it was impossible to obtain such quantitative information in previously reported studies. We believe that this improvement is primarily a result of the realization of a novel data preprocessing/optimization scheme for accurately determining several critical parameters needed for reconstruction. The use of this data preprocessing/optimization scheme also eliminates the calibration reference measurement previously required for reconstruction. Experimental confirmation of this scheme is given in detail. © 2000 Optical Society of America

OCIS codes: 170.3010, 170.3830, 170.3890, 170.6960.

1. Introduction

Near-infrared diffusive light can be used to image thick tissues such as breast and brain, as shown by recent significant progress in the area of optical imaging.[1-3] Among various optical methods that are being developed, reconstruction-based optical imaging has received particular attention because it can extract both structural and functional information from tissue. To date various reconstruction algorithms have been tested and evaluated by using considerable experimental data from different hardware systems including cw, frequency, and time domain.[4-17] Although significant progress has been made, a critical need to explore and improve reconstruction-based optical imaging performance in experimental conditions remains.

We are interested in frequency-domain systems in part because of the presence of a measurable phase component that can be exploited during image formation as well as cw or dc systems because of the added simplicity of recording only intensity data. When

The authors are with the Department of Physics and Astronomy, Biomedical Optics Laboratory, Clemson University, Clemson, South Carolina 29634-0978. H. Jiang's e-mail address is hjiang@clemson.edu.

powerful finite element-based reconstruction algorithms were used,[18] quantitative reconstruction of both absorption and scattering images has been achieved from frequency-domain measurements.[7,19-21] From dc data, simultaneous recovery of both absorption and scattering images has been obtained, but quantitative reconstruction in terms of optical property values was impossible.[22,23] In these early studies we used a calibration procedure based on a homogeneous medium measurement to calibrate the boundary conditions (BC's) and the source term. Although it was straightforward to do so, a trial-and-error process was needed to complete this calibration procedure. We found that the amplitude of the source largely determined the computed photon density amplitude and that BC's could affect the computed overall light distribution considerably, which suggests that this time-consuming procedure may introduce significant errors into the reconstruction if not carefully done. More important, it may not be practical to perform such a calibration measurement in an *in vivo* setting. We also believe that the inaccuracy caused by this calibration procedure made it impossible to obtain quantitative reconstruction from dc data, as confirmed by this study.

Although hampered by the requirement of a calibration measurement in the past few years, we have recently realized a novel data preprocessing/optimization scheme that allows for accurately determining the critical parameters needed for reconstruction including the BC coefficient, the excitation source term,

and the initial estimates of optical properties without reference or calibration measurements. In this paper we present in detail an experimental confirmation of this new scheme by using dc measurements. In addition, we demonstrate that the use of this scheme allows for quantitative-recovery of both absorption and scattering images from dc-only measurements. Experiments with tissuelike phantoms in both single-target and multitarget configurations have been performed where variations in target size and optical contrast with the background have been explored.

2. Methods and Materials

A. Data Preprocessing/Optimization Scheme

We have used in our study a finite-element-based algorithm for image reconstruction that has been previously described in detail.[18,19] The algorithm uses a regularized Newton method to update an initial (guess) optical property distribution iteratively to minimize an object function composed of a weighted sum of the squared difference between computed and measured data. To illustrate the data preprocessing/optimization scheme, here we briefly outline our reconstruction algorithm.

Since in this paper we focused on reconstruction by using dc data, our image reconstruction algorithm is based on the steady-state diffusion equation, which can be stated as

$$\nabla \cdot D(r)\nabla\Phi(r) - \mu_a(r)\Phi(r) = -S(r), \qquad (1)$$

where $\Phi(r)$ is the photon density, $\mu_a(r)$ is the absorption coefficient, and $D(r)$ is the diffusion coefficient, which can be written as $D(r) = 1/3[\mu_a(r) + \mu_s'(r)]$, where $\mu_s'(r)$ is the reduced scattering coefficient. $S(r)$ is the source term. In this study, a point source, $S = S_0\delta(r - r_0)$, is used in which S_0 is the source strength and $\delta(r - r_0)$ is the Dirac delta function for a source at r_0.

It has been shown that the following type III BC's can provide the most accurate solution of Eq. (1)[19,24]:

$$-D\nabla\Phi \cdot \hat{n} = \alpha\Phi, \qquad (2)$$

where $\hat{n}$ is the unit normal vector for the boundary surface and α is a coefficient related to the internal reflection at the boundary.

Making use of a finite element discretization, we can obtain a discrete matrix for Eq. (1) and realize other derived matrix relations through differentiation, which lead to a set of equations capable of an inverse problem solution[7,18,19]:

$$[A]\{\Phi\} = \{b\}, \qquad (3)$$

$$[A]\left\{\frac{\partial\Phi}{\partial\chi}\right\} = \left\{\frac{\partial b}{\partial\chi}\right\} - \left[\frac{\partial A}{\partial\chi}\right]\{\Phi\}, \qquad (4)$$

$$(\mathfrak{F}^T\mathfrak{F} + \lambda I)\Delta\chi = \mathfrak{F}^T[\Phi^{(m)} - \Phi^{(c)}], \qquad (5)$$

where the elements of matrix $[A]$ are $a_{ij} = \langle -D\nabla\phi_j \cdot \nabla\phi_i - \mu_a\phi_j\phi_i\rangle$, where $\langle\,\rangle$ indicates integration over the

problem domain; ϕ_i and ϕ_j are locally spatially varying Lagrangian basis functions at nodes i and j, respectively; χ expresses D or μ_a; $\mathfrak{F}$ is the Jacobian matrix that should be formed by $\partial\Phi/\partial\chi$ at the boundary measurement sites; $\Delta\chi = (\Delta D_1, \Delta D_2, \ldots, \Delta D_N, \Delta\mu_{a,1}, \Delta\mu_{a,2}, \ldots, \Delta\mu_{a,N})^T$ is the update vector for the optical property profiles, where N is the total number of nodes in the finite element mesh used; $\Phi^{(m)} = [\Phi_1^{(m)}, \Phi_2^{(m)}, \ldots, \Phi_M^{(m)}]$ and $\Phi^{(c)} = [\Phi_1^{(c)}, \Phi_2^{(c)}, \ldots, \Phi_M^{(c)}]$, where $\Phi_i^{(m)}$ and $\Phi_i^{(c)}$, respectively, are measured and calculated data for $i = 1, 2, \ldots, M$ boundary locations. Note that to estimate D and μ_a spatially, we need to expand these quantities in a similar manner to Φ as a finite sum of unknown coefficients multiplied by the locally defined Lagrangian basis functions.

In optical image reconstruction, the goal is to update the D and μ_a distributions through the solution of Eqs. (3)–(5) so that a weighted sum of the squared difference between computed and measured data can be minimized. Note that four critical parameters (the BC coefficient α, the source strength S_0, and the initial guesses of D and μ_a) must be accurately determined to obtain high-quality reconstructions. α is related to reflection at the tissue–air–detector interface; it is impossible to obtain an analytic expression of α for a realistic situation, particularly for an *in vivo* sitting. Although in principle S_0 can be measured, in a realistic situation it is time-consuming and inaccurate to do so. Although it is usually possible to make a good initial estimate of D and μ_a for laboratory experiments, it will be difficult to make such estimates in clinical situations. As indicated in Section 1, our early research in this regard had to rely on calibration measurements on a homogeneous medium to determine these critical parameters. Here we show that we can use a simple least-squares minimization scheme to determine these parameters accurately.

To illustrate this scheme, we show how one can determine the BC coefficient α. (The source term and initial estimates of the optical properties can be calculated in the same manner.) We compute the X^2 value as a function of α,

$$X^2 = \sum_{i=1}^{M} [\Phi_i^{(m)} - \Phi_i^{(c)}]^2,$$

where M is the number of boundary measurements, $\Phi_i^{(m)}$ is the measured photon density from a given experimental inhomogeneous medium, and $\Phi_i^{(c)}$ is the computed photon density from a numerical simulation of a homogeneous medium with the same geometry as the experimental medium. To calculate $\Phi_i^{(c)}$, we need to give only a range of the α value that covers the correct BC coefficient. With the given α each time, we compute $\Phi_i^{(c)}$ from Eq. (3). The rationale of this scheme is based on the argument that the minimum of X^2 corresponds to the correct value of α associated with the experimental inhomogeneous medium. In the same manner the source term and initial estimates of the optical properties can also be

Fig. 1. Schematic representation of the experimental setup.

B. Experimental Procedures and Parameters

computed. Note that this scheme is suitable for all data types including dc, frequency-, and time-domain data.

Our experimental setup, shown in Fig. 1, is an automated multichannel frequency-domain system that has been described in detail elsewhere.[25] With this system a radio-frequency intensity-modulated near-infrared beam at 785 nm is sent to the phantom by 16 fiber optic bundles coupled with a high-precision moving stage. The diffused light is received by another 16 channel fiber optic bundles and delivered to a photomultiplier tube (PMT). A second PMT is used to record the reference signal. These PMT's are supplied at a radio-frequency modulated current with a 0.1–1-kHz shift. The intermediary frequency signal obtained from the PMT's is processed with a National Instruments board. To increase the dynamic range of intensities that the PMT can detect, an automated filter wheel with precalibrated neutral density filters is added to the system. For every source position, 16 measurements for each detector were made, taking alternately 100-ms samples for sample and reference signals. The dc, ac, and phase shift between reference and sample signals were obtained by fast Fourier transform Labview routines. The total data collection time for 256 measurements was 8 min. We used only measured dc data to reconstruct the absorption and scattering images in this study.

In our experiments we used a 50-mm-diameter cylindrical solid phantom (1% Intralipid + India ink + Agar) as the background medium. In the cases examined the absorption coefficient μ_a of the background varied from 0.0005/mm to 0.005/mm, while the reduced scattering coefficient μ_s' was always 1.0/mm. Both single- and two-target configurations were used. In the single-target cases, target sizes of 15.0, 7.0, and 4.0 mm were examined. In the two-target case, one target 6.0 mm in diameter and one 8.0 mm in diameter were embedded in the background. The μ_a of the target varied from 0.015/mm to 0.050/mm; the μ_s' of the target was 1.0, 1.25, or 1.50/mm. The two-dimensional finite element mesh used had 249 nodes and 448 elements for both forward and inverse solutions. Note that here we do

Fig. 2. (a) Three-dimensional plot of the X^2 error versus the BC coefficient α and absorption coefficient μ_a. (b) X^2 error versus the BC coefficient α at a different absorption coefficient. (c) X^2 error versus source strength. (d) Reconstructed μ_a image. (e) Target/background geometry and reconstructed profile of μ_a along the cut-line, AB. In this case a 15-mm single target with $\mu_s' = 1.0$/mm and $\mu_a = 0.020$/mm was embedded in a background with $\mu_s' = 1.0$/mm and $\mu_a = 0.0005$/mm.

not need to use the dual-mesh scheme as used before[20,21] to obtain quantitative reconstruction by dc data. All the reconstructions were results of 20 iterations, after which no noticeable improvement was observed. The computations were performed on a 400-MHz Pentium II personal computer.

3. Results and Discussion

A series of experiments was conducted to evaluate the capabilities of our improved reconstruction algorithm to detect heterogeneities in the presence of single and multiple targets with different sizes and contrasts relative to the background. Both color-scale images reconstructed and quantitative plots of one-dimensional profiles of the exact and recovered property distributions contained in these images are presented in this section.

Through a simple single-target experiment, in Fig. 2 we present detailed results from data preprocessing/optimization. In this case the target was an absorber with only $\mu_a = 0.02$/mm. Figure 2(a) shows a three-dimensional plot of the X^2 error versus the BC coefficient α and the initial estimate value of μ_a. (Because we used the same μ_s' for the target and

background in this study, we easily found its value to be 0.99/mm by using this preprocessing procedure.) As can be seen, a minimum value of the X^2 error is clearly reached at $\alpha = 0.55$ and $\mu_a = 0.002$/mm. To examine this three-dimensional plot closely, one-dimensional profiles of the X^2 error as a function of α are provided at a different value of μ_a in Fig. 2(b). Again, the minimum is confirmed. Here when $\Phi_i^{(c)}$ (the photon density for a numerical simulation homogeneous medium with the same geometry as the experimental medium) was computed, the source term in Eq. (1) was already normalized with the highest photon density at the boundary. With the optimal values of α and μ_a determined, the optimal source strength S_0 can now be obtained by computing $\Phi_i^{(c)}$ with an unnormalized source term in Eq. (1). Figure 2(c) gives the result from this calculation in which the minimum of the X^2 error is reached at $S_0 = 49,500$ photons/mm^3/s. Using these values of critical parameters determined from the data preprocessing/optimization scheme, we reconstructed the absorption image as shown in Fig. 2(d). The absorption profile along the cut line AB is displayed in Fig. 3(e). It is clear that the recovered image is quantitative in terms of the optical property value, target location, and size.

Figure 3 shows the results from another two sets of experiments with the same target configuration as the case above but with different values of μ_a [0.015/mm in Figs. 3(a) and 3(b) and 0.035/mm in Figs. 3(c) and 3(d)]. As can be seen in Figs. 3(a) and 3(c), the minimum error was reached at $\alpha = 0.553$ and $\mu_a = 0.004$/mm and at $\alpha = 0.540$ and $\mu_a = 0.0075$/mm, respectively. These values of α and μ_a were then used to obtain the optimal source strength values. The reconstructed optical images and the target absorption profiles are shown in Figs. 3(b) and 3(d). As shown, the images are quantitatively reconstructed in terms of the localization, size, and optical properties of the target.

The capability of our improved algorithm to reconstruct a small target with both μ_a and μ_s' different from the background values is examined in Fig. 4. In this experiment a 4.0-mm-diameter target with $\mu_s' = 1.25$/mm and $\mu_a = 0.050$/mm was embedded in the background medium with $\mu_s' = 1.0$/mm and $\mu_a = 0.0005$/mm. Both reconstructed images and property profiles for both μ_s' and μ_a are presented in Fig. 4. Note that the μ_s' image can be recovered quantitatively even though its contrast with the background is low (1.25:1). The boundary artifacts appearing in the scattering image could be partially due to the a small-target perturbation that in this case led to overall low signal sensitivity for the reconstruction. The inherent ill-conditioned nature for the inverse problem that we have here makes it difficult to recover absorption and scattering images simultaneously. It appears to be generally more difficult for the scattering image to be reconstructed than the absorption image.[20,23]

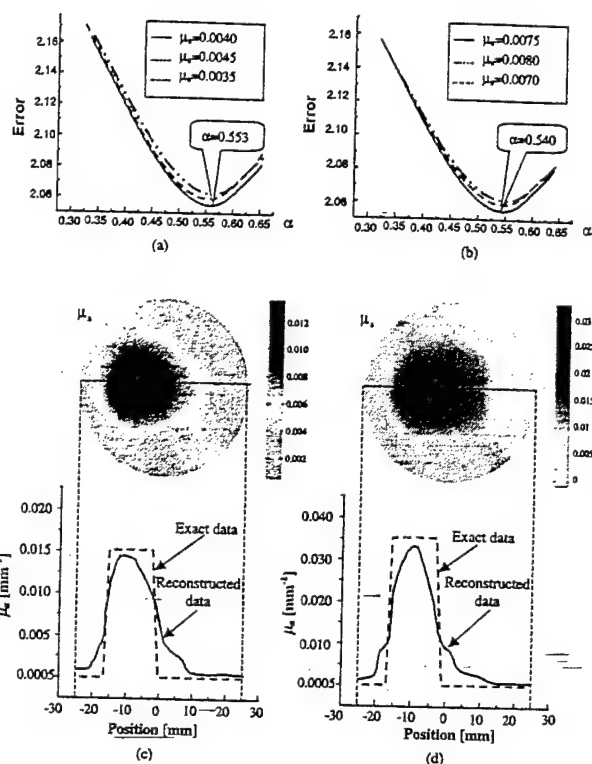In Fig. 5 are displayed the reconstructed images and the property profiles in which two differently

Fig. 3. (a) X^2 error versus the BC coefficient α at a different absorption coefficient. (b) Reconstructed μ_a image and profile along the cut-line AB. (c) X^2 error versus the BC coefficient α at a different absorption coefficient. (d) Reconstructed μ_a image and profile along the cut-line, AB. The background optical properties for these two cases are $\mu_s' = 1.0$/mm and $\mu_a = 0.0005$/mm. The optical properties of the 15-mm target are $\mu_s' = 1.0$/mm and $\mu_a = 0.015$/mm for (a) and (b) and $\mu_s' = 1.0$/mm and $\mu_a = 0.035$/mm for (c) and (d), respectively.

sized (6- and 8-mm) targets were embedded in the background medium ($\mu_s' = 1.0$/mm and $\mu_a = 0.0005$/mm). The two targets have the same μ_s' as
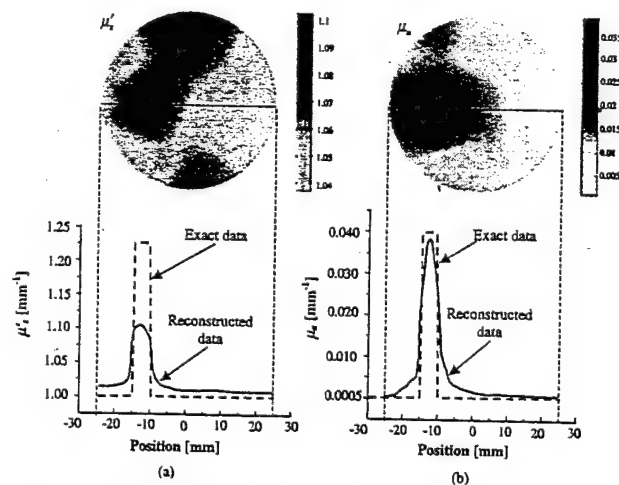

Fig. 4. Reconstructed μ_s' and μ_a images and their profiles along the cut-line, AB, for a 4-mm target that was embedded in the background with $\mu_s' = 1.0$/mm and $\mu_a = 0.0005$/mm. The target optical properties were $\mu_s' = 1.25$/mm and $\mu_a = 0.040$/mm.
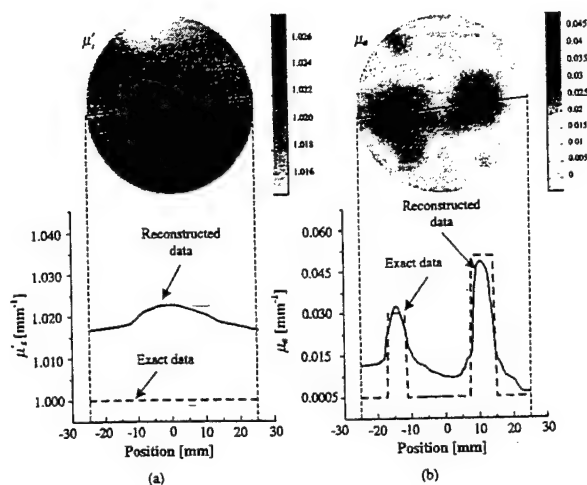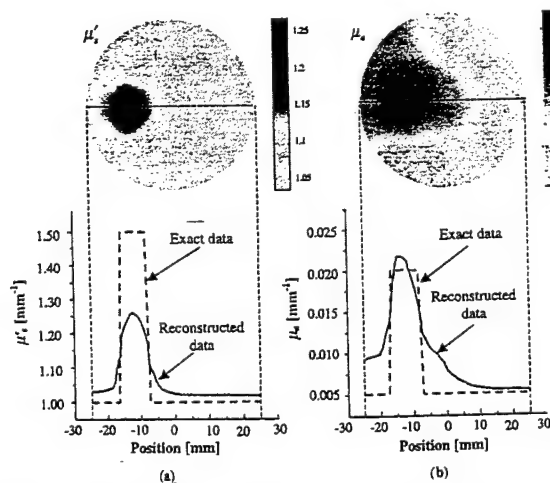
Fig. 5. Reconstructed μ_s' and μ_a images and their profiles along the cut-line, AB, for two differently sized (6- and 8-mm) targets that were embedded in the background with $\mu_s' = 1.0$/mm and $\mu_a = 0.0005$/mm. The left 6-mm target was $\mu_s' = 1.0$/mm and $\mu_a = 0.030$/mm, and the right 8-mm target was $\mu_s' = 1.0$/mm and $\mu_a = 0.050$/mm.

the background but different μ_a (0.030/mm for the left 6-mm target and 0.050/mm for the right 8-mm target). As can be seen, both targets can be clearly detected quantitatively in terms of the optical property value, size, and location of the targets.

The last experiment was a configuration in which a 10-mm target with both μ_a and μ_s' different from the background was embedded in a background with a larger μ_a (0.005/mm) than that of the background used in the previous cases. The background had $\mu_s' = 1.0$/mm. The target had $\mu_s' = 1.5$/mm and $\mu_a = 0.020$/mm. The reconstructed images and property profiles for both μ_a and μ_s' are presented in Fig. 6. Again, quantitative reconstructions are in evidence. Note from Figs. 4 and 6 that, although the low-

Fig. 6. Reconstructed μ_s' and μ_a images and their profiles along the cut-line, AB, for a 10-mm target that was embedded in the background with $\mu_s' = 1.0$/mm and $\mu_a = 0.0050$/mm. The target optical properties were $\mu_s' = 1.5$/mm and $\mu_a = 0.020$/mm.

contrast μ_s' images can be quantitatively recovered, it is difficult for the μ_s' profiles to fully reach their exact values. In contrast, the μ_a profiles can fully reach their exact values. We encountered the same situation in image reconstructions using frequency-domain data.[19–21] Although further study is warranted in this regard, we suspect that there is a mathematical competition between μ_s' and μ_a due to their own unique positions in the diffusion equation. Improvement in image quality may be realized if we consider this competition in the reconstruction algorithm.

4. Conclusions

We have demonstrated that the quantitative good reconstruction of absorption and scattering images can be achieved with dc data only. A series of experiments with both single-target and multitarget configurations has been conducted to evaluate our improved reconstruction algorithm. The data preprocessing/optimization scheme developed has been examined in detail. This scheme allows us to determine accurately all the critical initial parameters needed for reconstruction: the BC coefficient related to the tissue–detector–air interface, the source term associated with the model mismatch, and the initial estimates that are critical for a nonlinear optimization-based algorithm. In a practical situation, such as an *in vivo* measurement, the tissue–detector–air interface can be quite complicated; using the previous calibration procedure[19–21] to obtain an accurate BC coefficient is difficult. In fact such a calibration procedure requires a homogeneous medium measurement, which is impossible in a clinical situation. Similarly, when one wants to reconstruct a two-dimensional image from measurements performed in an actual three-dimensional sitting, the model mismatch always exists. This study shows that the proposed simple data preprocessing procedure can minimize the difference owing to this model mismatch. Finally this procedure also reduces computation cost significantly because it allows us to use a coarse single finite element mesh for both forward and inverse procedures.

References

1. B. Tromberg, A. Yodh, E. Sevick-Muraca, and D. Pine, "Diffusing photons in turbid media: introduction," Appl. Opt. **36**, 9 (1997).
2. A. Yodh, B. Tromberg, E. Sevick-Muraca, and D. Pine, "Diffusing photons in turbid media: introduction," J. Opt. Soc. Am. A **14**, 136 (1997).
3. B. W. Pogue, "Diffusion optical tomography: introduction," Opt. Express **4**, 1 (1999), http://epubs.osa.org/opticsexpress.
4. R. L. Barbour, H. Graber, J. Chang, S. Barbour, P. Koo, and R. Aronson, "MRI-guided optical tomography: prospects and

computation for a new imaging method," IEEE Comput. Sci. Eng. **2,** 63–77 (1995).

5. S. R. Arridge and M. Schweiger, "Image reconstruction in optical tomography," Philos. Trans. R. Soc. London Ser. B **352,** 717–726 (1997).

6. M. A. O'Leary, D. A. Boas, B. Chance, and A. G. Yodh, "Experimental images of heterogeneous turbid media by frequency-domain diffusing-photon tomography," Opt. Lett. **20,** 426–428 (1995).

7. H. Jiang, K. D. Paulsen, U. L. Osterberg, B. W. Pogue, and M. S. Patterson, "Simultaneous reconstruction of absorption and scattering profiles in turbid media from near-infrared frequency-domain data," Opt. Lett. **20,** 2128–2130 (1995).

8. H. Jiang, "Optical image reconstruction based on the third-order diffusion equations," Opt. Express **4,** 241–246 (1999), http://epubs.osa.org/opticsexpress.

9. W. Cai, S. Gayen, M. Xu, M. Zevallos, M. Alrubaiee, M. Lax, and R. Alfano, "Optical tomographic image reconstruction from ultrafast time-sliced transmission measurements," Appl. Opt. **38,** 4237–4246 (1999).

10. S. B. Colak, D. Papaioannou, G. tHooft, M. vander Mark, H. Schomberg, J. Paasschens, J. Melissen, and N. van Asten, "Tomographic image reconstruction from optical projections in light diffusing media," Appl. Opt. **36,** 180–213 (1997).

11. S. A. Walker, S. Fantini, and E. Gratton, "Image reconstruction by backprojection from frequency-domain optical measurements in highly scattering media," Appl. Opt. **36,** 170–179 (1997).

12. B. W. Pogue, T. McBride, J. Prewitt, U. Osterberg, and K. Paulsen, "Spatially variant regularization improves diffuse optical tomography," Appl. Opt. **38,** 2950–2961 (1999).

13. C. L. Matson and H. Liu, "Analysis of the forward problem with diffuse photon density waves in turbid media by use of a diffraction tomography model," J. Opt. Soc. Am. A **16,** 455–466 (1999).

14. J. Scotland, "Continuous-wave diffusion imaging," J. Opt. Soc. Am. A **14,** 275–279 (1997).

15. X. Cheng and D. Boas, "Diffuse optical reflection tomography with continuous-wave illumination," Opt. Express **3,** 118–123 (1998), http://epubs.osa.org/opticsexpress.

16. M. J. Eppstein, D. Dougherty, T. Troy, and E. Sevick-Muraca, "Biomedical optical tomography using dynamic parameterization and Bayesian conditioning on photon migration measurements," Appl. Opt. **38,** 2138–2150 (1999).

17. J. C. Ye, K. Webb, R. Millane, and T. Downar, "Modified distorted Born iterative method with an approximate Frechet derivative for optical diffusion tomography," J. Opt. Soc. Am. A **16,** 1814–1826 (1999).

18. K. D. Paulsen and H. Jiang, "Spatially varying optical property reconstruction using a finite-element diffusion equation approximation," Med. Phys. **22,** 691–702 (1995).

19. H. Jiang, K. Paulsen, U. Osterberg, B. Pogue, and M. Patterson, "Optical image reconstruction using frequency-domain data: simulations and experiments," J. Opt. Soc. Am. A **13,** 253–266 (1996).

20. H. Jiang, K. Paulsen, U. Osterberg, and M. Patterson, "Frequency-domain optical image reconstruction in heterogeneous media: an experimental study of single-target detectability," Appl. Opt. **36,** 52–63 (1997).

21. H. Jiang, K. Paulsen, U. Osterberg, and M. Patterson, "Frequency-domain near-infrared photo diffusion imaging: initial evaluation in multitarget tissuelike phantoms," Med. Phys. **25,** 183–193 (1998).

22. H. Jiang, K. Paulsen, and U. Osterberg, "Optical image reconstruction using DC data: simulations and experiments," Phys. Med. Biol. **41,** 1483–1498 (1996).

23. H. Jiang, K. Paulsen, U. Osterberg, and M. Patterson, "Improved continuous light diffusion imaging in single- and multitarget tissuelike phantoms," Phys. Med. Biol. **43,** 675–693 (1998).

24. R. Kaskell, L. Svaasand, T. Tsay, T. Feng, M. McAdams, and B. Tromberg, "Boundary conditions for the diffusion equation in radiative transfer," J. Opt. Soc. Am. A **11,** 2727–2741 (1994).

25. N. Iftimia and H. Jiang, "Development of a combined optical and fluorescence imaging system in frequency domain for breast cancer detection," in *Biomedical Topical Meetings,* Postconference Digest, Trends in Optics and Photonics Series (Optical Society of America, Washington, D.C., 2000), pp. 383–385.

Combined Optical and Fluorescence Imaging for Breast Cancer Detection and Diagnosis

Huabei Jiang,* Sathappan Ramesh, and Matthew Bartlett

Biomedical Optics Laboratory, Department of Physics and Astronomy, Clemson University, Clemson, SC 29634-1911

*Author to whom all correspondence should be addressed.

ABSTRACT: In this article, we present a novel approach that combines the best aspects of both endogenous optical imaging and exogenous fluorescent lifetime and yield imaging for breast cancer detection and diagnosis. Using this approach, spatial distributions of optical properties, fluorescence lifetime, and yield in tissue can be reconstructed from measured excitation and emission data at the surface of the breast tissue by regularized inverse algorithms. We show images from simulated data, as well as images from experimental data using tissue-like phantom materials in the laboratory.

KEY WORDS: optical imaging, fluorescence imaging, frequency-domain, breast cancer.

I. INTRODUCTION

X-ray mammography is the clinical tool currently used for breast cancer detection. However, mammography is ionizing radiation and has an unacceptable false-negative rate for patients with radiodense breast tissues. These patients represent the general population of premenopausal women as well as those with fibrocystic tissue disease. Yet, cancer in younger women tends to be more virulent and grow faster. Consequently, there is a critical need to seek alternatives that could overcome the problems associated with X-ray mammography and that could become an excellent adjunct or competitive tool to conventional X-ray mammography. Nonionizing, noninvasive optical imaging has great potential to become one of the most promising alternative strategies for breast cancer detection. This is underscored by the fact that in the last few years significant progress has been made in understanding the fundamental nature of light propagation in tissue, which has led to the emergence of several advanced techniques for transmission of light through tissue over distances relevant to breast imaging.[1] Considerable effort has

been made toward the realization of a new class of breast cancer detection methods using these emerging optical techniques.

Both direct imaging and image reconstructions using multiply scattered light have been demonstrated, largely from simulations and tissue phantom experiments. The majority of these optical imaging techniques employ methodologies that are based on differences in the absorption and/or scattering properties between the embedded object and its surroundings. While in vitro studies show that the endogenous optical contrast between the tumor and normal tissues can be quite low,[2] in vivo experiments indicate that this endogenous optical contrast can be as high as fourfold.[3] Nonetheless, development of methods for improving both the sensitivity and specificity for detection is necessary. Fluorescence spectroscopy/imaging studies of human tissue suggest that a variety of lesions show distinct fluorescence spectra compared with those of normal tissue.[4-7] It has been shown that exogenous dyes may offer the best contrast for optical imaging.[8-9] Use of exogenous agents would provide fluorescent markers that could serve to detect embedded tumors in the breast. In particular, the ability to monitor the fluorescent yield and lifetime may also provide biochemical specificity if the fluorophore is sensitive to a specific metabolite, such as oxygen, glucose, etc.[10] This has intrinsic merit that extends beyond the structural information contained in the static images associated with X-ray mammography, thus provides another strong rationale for its complementary role in the detection/diagnosis of breast cancer. Because tumors exhibit distinctive metabolite alternations, this ability to extract tissue functional information may offer a unique way for noninvasively differentiating between benign and malignant tumors.

In this paper, we present a novel approach that combines the best aspects of both endogenous optical imaging and exogenous fluorescent lifetime and yield imaging for breast cancer detection and diagnosis. Using this approach, spatial distributions of optical properties, fluorescence lifetime, and yield in tissue can be reconstructed from measured excitation and emission data at the surface of the breast tissue by regularized inverse algorithms. We report images from simulated data, as well as images from experimental data using tissue-like phantom materials in the laboratory.

II. THEORETICAL AND EXPERIMENTAL METHODS

In frequency-domain, it is known that propagation of both excitation and fluorescent emission light in tissues or multiply scattering media can be described by the following coupled diffusion equations:[11]

$$\nabla \cdot \left[D_x(r) \nabla \Phi_x(r, \omega) \right] - \left[\mu_{a_x}(r) - \frac{i\omega}{c} \right] \Phi_x(r, \omega) = -S(r, \omega) \qquad (1)$$

$$\nabla \cdot \left[D_m(r) \nabla \Phi_m(r, \omega) \right] - \left[\mu_{a_m}(r) - \frac{i\omega}{c} \right] \Phi_m(r, \omega) =$$

$$-\eta(r) \mu_{a_{x \to m}} \Phi_x(r, \omega) \frac{1 + i\omega\tau(r)}{1 + \omega^2 \tau(r)^2} \qquad (2)$$

where $\Phi x,m$ is the photon density for excitation (subscript x) or fluorescent light (subscript m), Dx,m is the diffusion coefficient, $\mu_{a_{x,m}}$ is the absorption coefficient due to contributions from both nonfluorescing chromophores and fluorescent dye, $\mu_{a_{x \to m}}$ is the absorption coefficient for the excitation light due to contribution from fluorescent dye, ω is the modulation frequency, c is the velocity of light in the medium, and η and τ are the fluorescent quantum yield and lifetime, respectively. $S(r, \omega)$ is the excitation source term in (1) which for a point source can be written as $S = So\delta(r - ro)$, where So is the source strength and $\delta(r - ro)$ is the Dirac-delta function for a source at ro. Note that a single-exponential fluorescence decay has been assumed in the source term for fluorescent light (right-hand side of (2)); multiexponential time decay can be handled by a simple extension. The diffusion coefficient can be written as $Dx,m(r) = 1/3[\mu_{a_{x,m}}(r) + \mu'_{s_{x,m}}(r)]$, where $\mu'_{s_{x,m}}(r)$ is the reduced scattering coefficient. For known optical properties and fluorescent lifetime and yield, Eqs. (1) and (2) become standard boundary value problems for the spatially varying photon densities of excitation and emission light subject to appropriate boundary conditions (BCs). We use the non-zero photon density BCs or type III BCs in this article, which are proved to be the most accurate ones:[12] $-D_{x,m} \nabla \Phi_{x,m} \cdot \hat{n} = \alpha \Phi_{x,m}$, where $\hat{n}$ is the unit normal vector for the boundary surface and α is a coefficient that is related to the internal reflection at the boundary.

In combined optical and fluorescence imaging, the goal is to recover all distributions, including Dx,m, $\mu_{a_{x,m}}$, τ, and η. Our image reconstruction algorithms are centered on the finite element method. The image formation algorithms cast the inverse problem associated with determining the optical and fluorescent characters of the medium (i.e., breast tissue) as a nonlinear parameter estimation where known excitations accompanied with measured data are used to find a "best fit" of the tissue optical and fluorescent parameters needed to reproduce the known information. The details of our reconstruction algorithms have been described in References 12 and 13.

The experimental system used for the combined optical and fluorescence imaging is a frequency-domain optical system that has been described in detail in Reference 12. Using the frequency-domain imaging system, the phase-shift and intensity for excitation and fluorescent light can be measured.

III. RESULTS AND CONCLUSIONS

For simulations, Figure 1 shows the lifetime and yield images reconstructed under conditions of no noise and with 5% added noise for the "measured" intensity
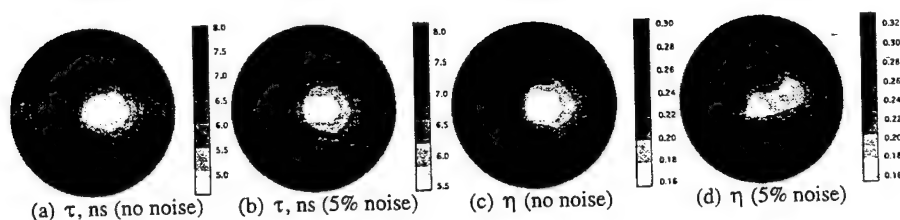
(a) τ, ns (no noise)   (b) τ, ns (5% noise)   (c) η (no noise)   (d) η (5% noise)

FIGURE 1.   Simulated simultaneous reconstruction of both fluorescent lifetime (τ, ns) and yield (η, dimensionless) under different noise condition. (a) τ reconstruction with no noise added; (b) τ reconstruction with 5% random noise added; (c) η reconstruction with no noise added; (d) η reconstruction with 5% random noise added. In these simulations, a 15-mm-diameter object is embedded in a 43-mm-diameter background region.

and phase shift of both excitation and emission light. As can be seen, the images formed are qualitatively correct, even for those with a 5% noise level. For experiments, Figure 2 presents optical property images reconstructed using tissue-like phantom materials that simulate soft tissues. Here we show that a 4-mm-size object can be clearly recovered using our reconstruction approach.

In summary, we have demonstrated optical and fluorescent image reconstructions using simulated and experimental data. Our results show that it is possible to detect breast tumors using our approach described here. At Clemson we are currently developing a clinical prototype imaging system for human subject studies.

ACKNOWLEDGMENTS

D, 8 mm Object   μ$_a$, 8 mm Object   D, 4 mm Object   μ$_a$, 4 mm Object
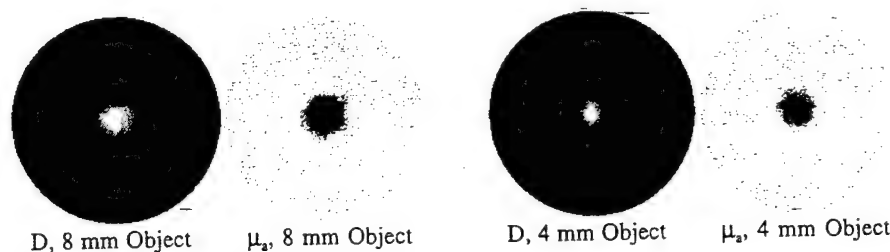
FIGURE 2.   Optical property images reconstructed from experimental data using tissue-like phantom materials (Intralipid mixed with India ink). The diameter of the background region is 86 mm. The data used were collected from the frequency-domain imaging system described in Reference 12.

REFERENCES

1. **Wilson, B. C., Sevick, E. M., Patterson, M. S., and Chance, B.**, Time-dependent optical spectroscopy and imaging for biomedical applications, *Proc. IEEE*, 80, 918–930, 1992.

2. **Troy, T., Page, D., and Sevick-Muraca, E.**, Optical properties of normal and diseased breast tissues: prognosis for optical mammography, *J. Biomed. Optics*, 1, 342–355, 1996.

3. **Tromberg, B. J., Coquoz, O., Fishkin, J., Pham, T., Anderson, E., Butler, J., Cahn, M., Gross, J., Venugopalan, V., and Pham, D.**, Noninvasive measurements of breast tissue optical properties using frequency-domain photon migration, *Phil. Trans. R. Soc. Lond. B*, 352, 661–668, 1997.

4. **Richards-Kortum, R., Rava, R. P., Fitzmaurice, M., Tong, L. L., Ratliff, N., Kramer, J., and Feld, M. S.**, A one layer model of laser-induced fluorescence for diagnosis of disease in human tissue: applications to atherosclerosis, **IEEE Trans. Biomed. Eng.**, 36, 1222–1232, 1989.

5. **Alfano, R. R., Tang, G. C., Pradhan, A., Lam, W., Choy, D. S., and Opher, E.**, Fluorescence spectra from cancerous and normal human breast and lung tissues, *IEEE J. Quantum Electron.*, QE-23, 1806–1811, 1987.

6. **Andersson, E. S., Johansson, J., Svanberg K., and Svanberg, S.**, Fluorescence imaging and point measurements of tissue: applications to the determination of malignant tumors and atherosclerotic lesions from normal tissue, *Photochem. Photobiol.*, 53, 807–814, 1991.

7. **Yang, Y.**, Fluorescence spectroscopy as a photonic pathology method for detecting colon cancer, *Lasers Life Sci.*, 6, 259–276, 1995.

8. **Troy, T., Nelson-Larry, L., Hutchinson, C. L., and Sevick-Muraca, E. M.**, Investigation of exogenous contrast agents for biomedical optical imaging, Proc. OSA Topical Meeting: *Biomedical Optical Spectroscopy and Diagnostics*, 1996, 104–106.

9. **Sevick-Muraca, E., Lopez, G., Troy, T., Reynolds, J., and Hutchinson, C.**, Fluorescence and absorption contrast mechanisms for biomedical optical imaging using frequency-domain techniques, *Photochem. Photobiol.*, 66, 55–64, 1997.

10. **Lakowicz, J. R.**, *Principles of Fluorescence Spectroscopy*, Plenum Press, New York, 1983.

11. **Li, X., O'Leary, M., Boas, D., Chance, B., and Yodh, A.**, Fluorescent diffuse photon density waves in homogeneous and heterogeneous turbid media: analytic solutions and applications, *Applied Optics*, 35, 3746–3758, 1996.

12. **Jiang, H., Paulsen, K. D., Osterberg, U. L., Pogue, B. W., and Patterson, M. S.**, Optical image reconstruction using frequency-domain data: simulations and experiments, *J. Optical Society Am. A*, 13, 253–266, 1996.

13. **Jiang, H.**, Frequency-domain fluorescent diffusion tomography: a finite element algorithm and simulations, *Appl. Opt.*, 37, 5337–5343, 1998.

Frequency-domain Fluorescent Diffusion Tomography of Turbid Media and *in vivo* Tissues

Ye Yang, Nicusor Iftimia, Yong Xu and Huabei Jiang

Biomedical Optics Lab, Department of Physics & Astronomy
Clemson University, Clemson, SC29634-0978

Keywords: Fluorescence lifetime tomography, Frequency domain, Biomedical optical imaging, Optical tomography, Image reconstruction, Diffusion tomography

ABSTRACT

The reconstruction of fluorescence lifetime distributions in heterogeneous turbid media and tumor-bearing animals are experimentally demonstrated by frequency-domain measurements. A set of coupled diffusion equations are used to describe the propagation of excitation and fluorescent emission light in multiply scattering media. A finite element based reconstruction algorithm combined with Marquardt and Tikhonov regularization methods are used to obtain the fluorescence images. The experimental set-up is an automatic multi-channel frequency-domain system. 16 sources and 16 detectors are used. Experiments are performed using indocyanine green (ICG) and 3,3'-diethylthiatricarbocyanine iodide (DTTCI) in tissue-like phantoms of both single- and multi-target configurations with considerations of perfect and imperfect uptake of fluorescence dyes in the scattering media. ICG are used in tumor-bearing animal studies. Our results show that the fluorescence lifetime image of the heterogeneities within a circular surrounding medium and *in-vivo* tissue can be reconstructed successfully.

1. INTRODUCTION

Recently the idea of reconstruction life-based fluorescence diffusion tomography has been proposed and developed for clinical applications such as breast cancer detection and tissue functional mapping.[1-6] This new imaging approach relies on the fact that the lifetime of fluorophores in tissue can potentially provide tissue functional information such as tissue oxygenation, pH, and glucose.[7] It is also based on the fact that the fluorophore will preferentially accumulate in tumors, hence providing the best sensitivity for cancer detection.[8] In this type of indirect imaging method, an effective reconstruction algorithm is crucial which allows for the formation of a spatial map of the lifetime of heterogeneous fluorophore distributions. To date fluorescence image reconstructions are largely limited to simulated data, based on linear and nonlinear algorithms.[1-6] Chang et al.[2] attempted to obtain a qualitatively good image of the fluorophore concentration only from dc measurements. In this paper we

present successful reconstruction of lifetime images from frequency-domain measurements using indocyanine green (ICG) dye and 3,3'-diethylthiatricarbocyanine iodide (DTTCI) in tissue-like phantoms of single- and multi-target configurations with considerations of perfect and imperfect uptake of fluorescence dyes in the scattering media. And ICG are used in tumor-bearing animal studies.

2. RECONSTRUCTION ALGORITHM

In frequency-domain, it is known that propagation of both excitation and fluorescent emission light in tissues or turbid media can be described by the following coupled diffusion equations:[2-6]

$$\nabla \cdot [D_x(r)\nabla\Phi_x(r,\omega)] - \left[\mu_{a_x}(r) - \frac{i\omega}{c}\right]\Phi_x(r,\omega) = -S(r,\omega) \tag{1}$$

$$\nabla \cdot [D_m(r)\nabla\Phi_m(r,\omega)] - \left[\mu_{a_m}(r) - \frac{i\omega}{c}\right]\Phi_m(r,\omega) = -\eta(r)\mu_{a_{x\to m}}\Phi_x(r,\omega)\frac{1+i\omega\tau(r)}{1+\omega^2\tau(r)^2} \tag{2}$$

where $\Phi_{x,m}$ is the photon density for excitation (subscript x) or fluorescent light (subscript m), $D_{x,m}$ is the diffusion coefficient, $\mu_{a_{x,m}}$ is the absorption coefficient due to contributions from both non-fluorescing chromophores and fluorescent dye, $\mu_{a_{x\to m}}$ is the absorption coefficient for the excitation light due to contribution from fluorescent dye, ω is the modulation frequency, c is the velocity of light in the medium, and η and τ are the fluorescent quantum yield and lifetime, respectively. $S(r,\omega)$ is the excitation source term in (1). Note that a single-exponential fluorescence decay has been assumed in the source term for fluorescent light (right-hand-side of (2)); multi-exponential time decay can be handled by a simple extension. The diffusion coefficient can be written as $D_{x,m} = 1/3(\mu'_{s_{x,m}} + \mu_{a_{x,m}})$ where $\mu'_{s_{x,m}}$ is the reduced scattering coefficient. In this study a point excitation source, $S = S_0\delta(r - r_0)$, and Type III boundary conditions (BCs): $-D_{x,m}\nabla\Phi_{x,m} \cdot \hat{n} = \alpha\Phi_{x,m}$, are used, where S_0 is the source strength, $\hat{n}$ is the unit normal vector for the boundary surface and α is a coefficient that is related to the internal reflection at the boundary. Both S_0 and α are determined directly from the heterogeneous measurements by use of a data pre-processing scheme that is reported elsewhere.[9]

In fluorescence lifetime tomography, the goal is to recover all distributions including $D_{x,m}$, $\mu_{ax,m}$, τ and η. We are focusing on the reconstruction of τ. Other parameters can be easily dealt with in the same way. Making use of finite element discretization, we can obtain two matrix equations for Eqs. (1)-(2) and realize other derived matrix relations through differentiation:

$$[A_x]\{\Phi_x\} = \{b_x\} \tag{3}$$

$$[A_m]\{\Phi_m\} = \{b_m\} \tag{4}$$

where the elements of matrices $[A_x]$ and $[A_m]$ are respectively $(a_{x,m})_{ij} = < -D_{x,m} \nabla \psi_j \cdot \nabla \psi_i - (\mu_{a_{x,m}} - \frac{i\omega}{c}) \psi_j \psi_i >$, and

the entries in column vectors $\{b_{x,m}\}$ and $\{\Phi_{x,m}\}$ are $(b_x)_i = - < S\psi_i > + \alpha \sum_{j=1}^{M} (\Phi_x)_j \oint \psi_j \psi_i ds$,

$(b_m)_i = - < \sum_{k=1}^{K} \eta_k \psi_k \mu_{a_{x\to m}} \sum_{j=1}^{N} (\Phi_x)_j \psi_j \psi_i (1 - i\omega \sum_{l=1}^{L} \tau_l \psi_l)/(1 + \omega^2 (\sum_{l=1}^{L} \tau_l \psi_l)^2) > + \alpha \sum_{j=1}^{M} (\Phi_m)_j \oint \psi_j \psi_i ds$, and

$\Phi_{x,m} = \{(\Phi_{x,m})_1, (\Phi_{x,m})_2, \cdots (\Phi_{x,m})_N\}^T$, where $\langle \ \rangle$ indicates integration over the problem domain, and $\Phi_{x,m}$, τ has been expanded as the sum of coefficients multiplied by a set of locally spatially-varying Lagrangian basis functions ψ_j, ψ_l and ψ_k. $\oint$ expresses integration over the boundary surface where Type III BCs have been applied. $(\Phi_{x,m})_i$ is the photon density at node i, N is the node number of a finite element mesh and M is the boundary node number.

To form images from presumably uniform initial guess, we use the following equation to update τ from their starting values.

$$\Im \Delta\tau = \Phi_m^{(o)} - \Phi_m^{(c)} \tag{5}$$

where $\Phi_m^{(o)}$ and $\Phi_m^{(c)}$ are the observed and computed fluorescent data, respectively. $\Im$ is the Jacobian matrix consisting of the derivatives of Φ_m with respective to τ at each boundary observation node; $\Delta\tau$ is the vector that expresses perturbations of τ.

But as the approximation of principle, the influence of coherent noise and system noise, the "ill-condition" of the equation (5) is almost inevitable. We use Marquardt and Tikhonov regularization methods to stabilize the decomposition of the square system of equations.

$$(\Im^T \Im + \lambda I)\Delta\tau = \Im^T (\Phi_m^{(o)} - \Phi_m^{(c)}) \tag{6}$$

where I is the identity matrix and λ maybe a scalar or a diagonal matrix.

When a weighted sum of the squared difference between computed and measured data is minimized, a lifetime image can be obtained.

3. EXPERIMENTS AND METHODS

3.1 Experimental Set-up

The basic components of our frequency-domain experimental set-up is shown in Fig. 1. The system used a near-infrared laser diode to provide excitation. The laser was modulated by a radio-frequency sine wave of frequency f that was amplified by RF
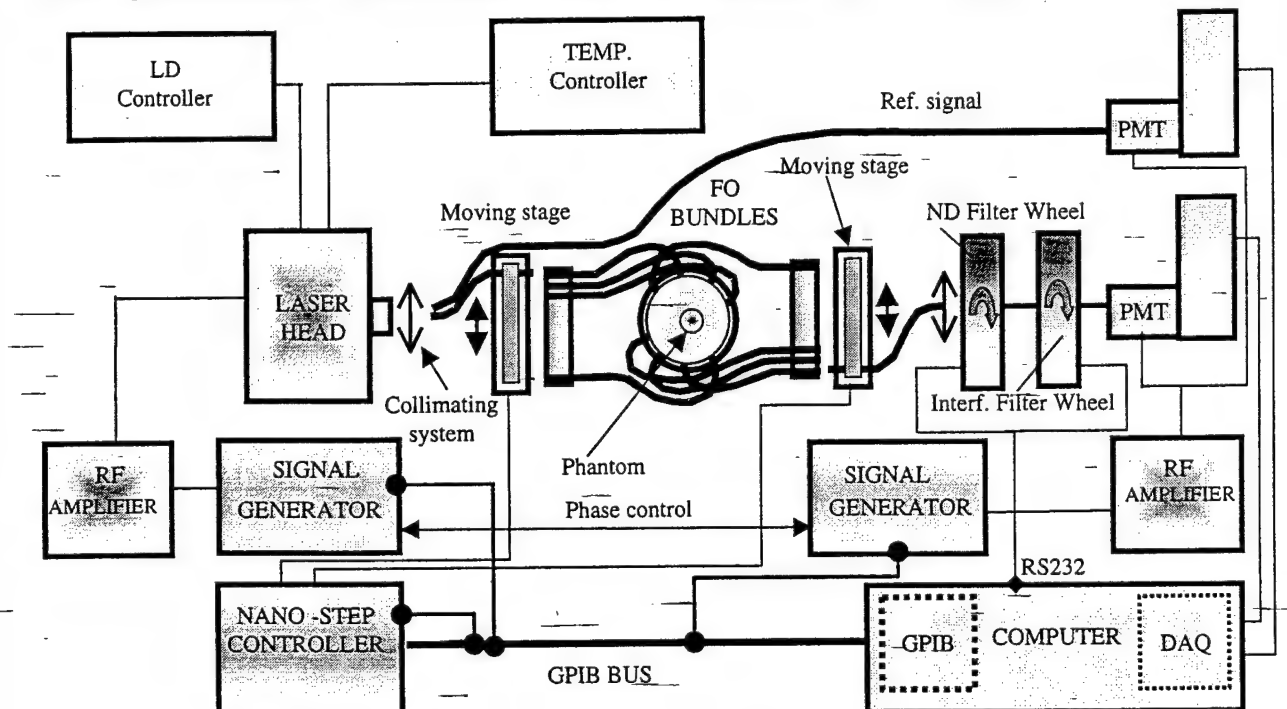

Fig. 1 Experimental Set-up

amplifier. The modulated light was collected by the collimating system and then focused down into the 2.47 mm core diameter fiber. 16 source fibers and 16 detect fibers are combined together to form a measuring a ring. The laser beam was sent to the phantom by 16 fiber optic bundles coupled with a high precision moving stage. The diffused radiation was received by another 16 channel fiber optic bundles and delivered to a PMT. A second PMT was used to record the reference signal. These PMTs were driven by another amplified synthesizer signal at a frequency of f +0.0001-0.001MHz . A heterodyning effect was achieved, which produced a 100Hz~1000Hz signal. Both reference signal and diffusion signals were digitized by a data acquisition board which is inserted in the expanded slot of the PC computer. In order to increase the system dynamic range, an automated filter wheel with pre-calibrated neutral density filters was added to the system. For every source position, diffusion and reference signals were taking alternatively for every detect fiber. Fluorescence signals were obtained through an interference filter, which was placed in front of the detection PMT. AC, DC intensities and phase shift between reference and diffusion signals were obtained using FFT Labview routines. For each measurement position, it would need about 100 ms to

acquire the data. For total 256 measurements, it would take about 8 minutes to complete the data collection. In animal experiments, only 11 source fibers and 11 detector fibers were used. The total time for 121 measurements were about 5 minutes.

3.2 Experimental methods

Solid phantom[10] was used to mimic the human tissue. It was made of agar, Intralipid, black ink and fluorescent dyes. The absorption and the reduced scattering coefficients are linear with the ink and Intralipid concentrations, respectively. Micromolar ICG and DTTCI dyes were added in the tissue phantom to provide the fluorescence contrast. Agar is used to make the phantom solid. The solid phantom is consisted of a cylindrical background and a cylindrical heterogeneity.

The absorption peaks of ICG and DTTCI are 764 nm and 780 nm, respectively. And the fluorescent emission peaks of them are 803 nm and 830 nm respectively. Their lifetimes in water are 0.56 ns and 1.18 ns, respectively.[8] A laser diode of wavelength 785 nm was used to excite both dyes, and the emission light of wavelength at 830 nm were detected for both of them through an interference filter of center wavelength 830 nm with 10nm bandwidth.

Wistar furth female rats with MT/W9a-B (mammary carcinosarcoma) cell line developed in their right udder were used as the animal models. Animals were studied when the tumor sizes were around 10~30 mm diameters. Animals were initially anesthetized with 2% isoflurane. The femoral vein was cannulated for the administration of intravenous drugs, including the dye ICG. Anesthesia was maintained during the experiment. The animals were placed in a holder with their tumor positions placed into the measuring ring. 1.5 mg/Kg bodyweight of ICG dye was injected into the animal. Imaging studies were carried out after 2 minutes of the dye injection.

3.3 Experimental Results

3.3.1   Phantom measurement results

Phantom studies were carried out with single and multi-targets configurations. Different dye concentration contrast, different absorption coefficient and size contrasts between the background and the heterogeneities were studied. Perfect (no dye was present in the background) and imperfect uptake (background with dye) of fluorescence dyes in the scattering media also were studied.

Figs. 1~5 show the reconstructed images of τ for phantoms with one or two off-centered targets . Figs.1~2 are the results of perfect uptake of the fluorescent dyes. Figs. 3~5 are the results of imperfect uptake of the fluorescent dyes, with lifetime of the target is shorter or longer than that of the background. As can be seen, all the targets can be clearly imaged. The targets' locations and sizes are also correctly resolved (exact data are not shown). It is also interesting to note that a finite value of τ (larger than the τ value in the target) for the background region is always reconstructed in the perfect uptake cases, although there is no fluorophore distribution in the background.

3.3.2   *In vivo* tissue measurement result

Fig. 6 shows a reconstructed image of τ for a tumor- bearing rat. The rat has a body size of 33 mm diameter and tumor size of 10 mm diameter. The weight of the rat is 155g. The reconstructed lifetime image shows that the lifetime in the tumor area is longer than the surrounding normal tissue. ICG dye is used in the animal studies. The reconstructed lifetime image shows the tumor size and location correctly (exact data are not shown).
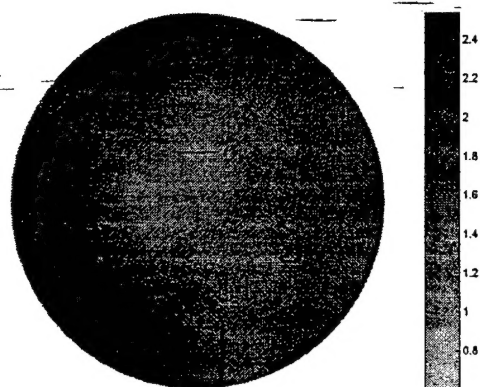

Fig. 1 Reconstructed lifetime image of phantom. The background hadn't dye inside and the target had ICG dye of concentration 0.5 μM. The diameter of the background and the target were 50.0 mm and 12.8 mm, respectively. The reduced scattering coefficients of the background and target were the same as 0.5 mm^{-1}. The absorption of the background and target were 0.001 mm^{-1} and 0.005 mm^{-1}, respectively. The lifetime of ICG in water is 0.56 ns.
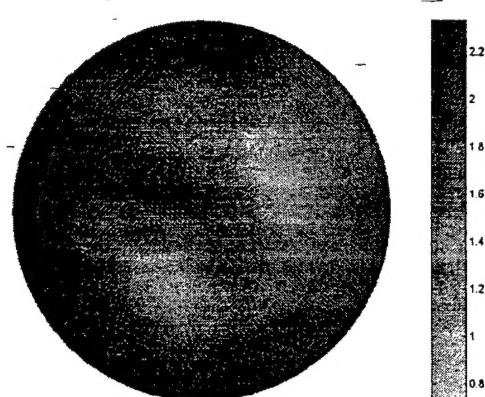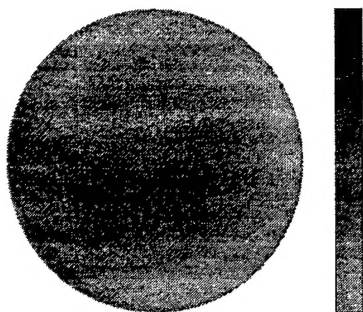
Fig. 2 Reconstructed lifetime image of phantom. The background hadn't dye inside and the targets had ICG dye of concentration 1.0 μM. The diameter of the background and the target were 50.0 mm and 10.0 mm, respectively. The reduced scattering coefficients of the background and target were the same as 0.5mm^{-1}. The absorption of the background and target were 0.001 mm^{-1} and 0.005 mm^{-1}, respectively. The lifetime of ICG in water is 0.56 ns.
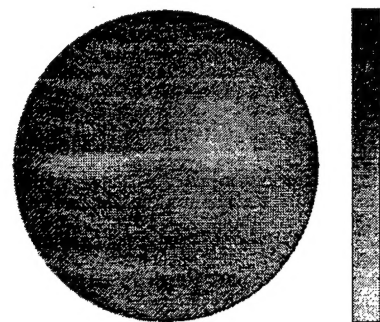
Fig. 3 Reconstructed lifetime image of phantom. The background had ICG dye of concentration 0.1 μM, and the target had DTTCI dye of concentration 5.0 μM. The diameter of the background and the target were 50.0 mm and 12.8 mm, respectively. The reduced scattering coefficients of the background and target were the same as 0.5 mm⁻¹. The absorption of the background and target were 0.001 mm⁻¹ and 0.005 mm⁻¹, respectively. The lifetimes of ICG and DTTCI in water are 0.56 ns and 1.18 ns, respectively.

Fig. 4 Reconstructed lifetime image of phantom. The background had DTTCI dye of concentration 0.1 μM, and the target had ICG dye of concentration 3.0 μM. The diameter of the background and the target were 35.0 mm and 8.5 mm, respectively. The reduced scattering coefficients of the background and target were the same as 0.5 mm⁻¹. The absorption of the background and target were 0.001 mm⁻¹ and 0.005 mm⁻¹, respectively. The lifetimes of ICG and DTTCI in water are 0.56 ns and 1.18 ns, respectively.
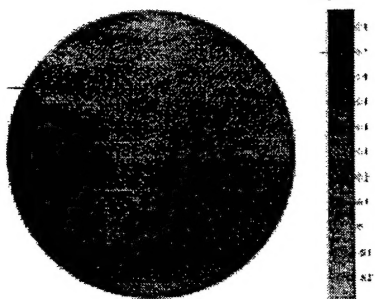

Fig. 5 Reconstructed lifetime image of phantom. The background had ICG dye of concentration 0.04 μM, and the target had DTTCI dye of concentration 1.21 μM. The diameter of the background and the target were 57.5 mm and 13.5 mm, respectively. The reduced scattering coefficients of the background and target were the same as 0.5 mm⁻¹. The absorption of the background and target were 0.005 mm⁻¹ and 0.01 mm⁻¹, respectively. The lifetimes of ICG and DTTCI in water are 0.56 ns and 1.18 ns, respectively.
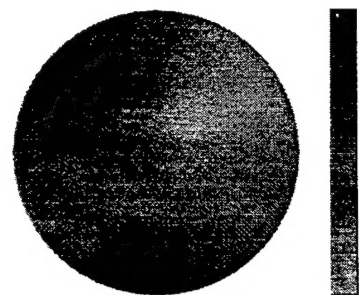
Fig. 6 Reconstructed lifetime image of tumor-bearing rat. The diameters of the tumor and the rat's body were 10mm and 33mm, respectively. The weight of the rat was 155g. The lifetime of ICG in water is 0.56 ns.

4 CONCLUSIONS

Fluorescence lifetime images reconstruction in turbid media and *in vivo* tissues were studied in this paper. Both single- and multi-target configurations with considerations of perfect and imperfect uptake of fluorescence dyes in scattering media were studied. *In-vivo* tissue lifetime image reconstruction were studied on tumor-bearing animals. The results showed that the fluorescence lifetime of the heterogeneities within a circular surrounding medium and *in-vivo* tissue can be reconstructed successfully using the algorithm and frequency-domain measurement presented in this paper.

REFERENCE

1. M. O'Leary, D. Boas, X. Li, B. Chance and A. Yodh, *Opt. Lett.* **21**, 158(1996).

2. J. Chang, H. Graber, R. Barbour, *JOSA A* **14**, 288(1997).

3. J. Chang, H. Graber, R. Barbour, *IEEE Trans. Biomed. Engr.* **44**, 810(1997).

4. D. Paithankar, A. Chen, B. Pogue, M. Patterson, E. Sevick-Muraca, *Appl. Optics* **36**, 2260(1997).

5. H. Jiang, *Appl. Opt.* **37**, 5337(1998).

6. R. Roy, E. Sevick-Muraca, *Opt. Express* **4**, 353(1999).

7. S. Bambot, J. Lakowitz, G. Rao, *Trands Biotechnol.* **13**, 106(1993).

8. E. Sevick-Muraca, G. Lopez, T. Troy, J. Reynolds, C. Hutchinson, *Photochemistry and Photobiology* **66**, 55(1997).

9. N. Iftimia, H. Jiang *Appl. Optics* **39**, 5256(2000).

10. R. Cubeddu, A. Pifferi, P. Taroni, A. Torricelli and G. Valentini, *Phys. Med. Biol.*, **42** (1997) 1971